THREE-DIMENSIONAL COMPUTATIONAL METHODS APPLIED TO AERODYNAMIC ANALYSIS OF TRANSONIC FLOWS PAST A WING-BODY CONFIGURATION.

By

B. CHAUMET (1), D. DESTARAC (1), T.H. LÊ (2)

Office National d'Etudes et de Recherches Aérospatiales (O.N.E.R.A.)

92320 CHATILLON - FRANCE

ABSTRACT

Since the first three-dimensional transonic computational methods based on the full potential equation were developed, considerable advancements have been made in the allowance for a number of aerodynamic effects. The purpose of the present paper is to analyse two of these effects : wing-body interaction (in inviscid flow) and viscous effects (on a wing alone).

The chosen configuration, DFVLR-F4, is a 1/38 scale model of an advanced supercritical wing mounted on an A310 fuselage.

The inviscid transonic flow past the wing-fuselage configuration is calculated by a multidomain method. The computational space is decomposed into two overlapping subdomains in which two grids well-suited to each of the components (wing and fuselage) are generated. The iterative algorithm solving the full potential equation is applied in a cyclic manner in the two domains, the two solutions being connected by the Schwarz alternating method.

The influence of the boundary layer on the wing alone is estimated by a three-dimensional inviscid-viscous method, coupling an inviscid FPE solver with an integral laminar-turbulent boundary layer method. The boundary layer effect is modelled after the defect formulation and wall transpiration velocity concept.

For a supercritical and a subcritical case, the separate effects of the fuselage and the boundary layer are estimated and described in terms of pressure and lift distributions ; modifications of the flow prediction by allowing for these effects are shown, as regards the pressure levels and the position and structure of the shock waves. The analysis also shows that the calculation - experiment correlation can be improved by more thorough modelling of experimental phenomena such as aeroelastic deformation of the wing and flow behaviour near the trailing edge.

NOMENCLATURE

b	: span
c	: local chord length
$\bar{c}$	: aerodynamic reference chord length
C_ℓ	: local section lift coefficient
C_L	: total lift coefficient
C_P	: pressure coefficient
H_i	: incompressible shape factor $\equiv \delta_{1i} / \theta_{11i}$
M	: freestream Mach number
$Re_{\bar{c}}$	: reference Reynolds number
u	: local boundary layer velocity in the external streamwise direction
u_e	: external velocity magnitude
x	: chordwise direction
y	: spanwise direction
z	: normal direction to the x,y plane
w	: wall transpiration velocity
α	: angle of attack
α_e	: angle between external streamline and x-z plane
β	: angle between external streamline and wall streamline
δ	: boundary layer thickness
δ_{1i}	: incompressible streamwise displacement thickness $\equiv \int_0^1 (1 - \frac{u}{u_e}) d(\frac{z}{\delta})$
η	: spanwise non-dimensional position $\equiv 2.y/b$
Λ	: aspect ratio
λ	: taper ratio
ω	: relaxation factor
ρ	: local density
ρ_e	: density at edge of boundary layer
θ_{11i}	: incompressible streamwise momentum thickness $\equiv \int_0^1 \frac{u}{u_e} (1 - \frac{u}{u_e}) d(\frac{z}{\delta})$
θ_{11}	: streamwise momentum thickness $\equiv \int_0^1 \frac{\rho u}{\rho_e u_e} (1 - \frac{u}{u_e}) d(\frac{z}{\delta})$

(1) Engineer, Applied Aerodynamics.
(2) Research Scientist, Theoretical Aerodynamics.

1 - INTRODUCTION -

Methods used to predict transonic flows around more or less complicated 3D aircraft configurations are (still) mostly based upon the full potential equation solution [1,2,3,4,5]. Generally, the potential approach is preferred to small disturbance, except when dealing with very complicated multicomponent configurations [6,7] which are often beyond capabi-

lities of the FPE methods. But, considering the recent development of fast 3D-Euler solvers [8] together with the use of vector computers, the Euler equations might in the future supersede the FPE in applied computational transonic aerodynamics as a standard approach. However, in many cases where strong shock waves are not involved, the potential approach used in this study is convenient. Moreover, there are other important limitations that may affect transonic methods whether they be based on the Euler equations or the potential approach. For example : a lack of accuracy or sophistication in modelling geometrical features of the configuration, or the inviscid flow assumption [9]. Understandably enough, consequences of these limitations have been shown to be highly dependent on the case being considered (fighter or transport aircraft configuration, supercritical or conventional wings, etc...) [10]. This paper aims at estimating how much the removal of the two above mentioned limitations may improve the theoretical prediction of transonic flows for an advanced transport configuration.

The test case described in section 2, an AIRBUS-type wing-fuselage configuration, has been chosen because its treatment by inviscid "wing alone" methods yields an inaccurate prediction of the flow [11]. The improvement thus needed has been sought by applying two methods available at ONERA which are described in section 3. They are both based on a full potential equation solver developed by CHATTOT. The first method, developed by LE, uses this solver as part of a multidomain method which allows the precise modelling of a flow around a two component configuration : a wing mounted on a fuselage of arbitrary shape. The second one, the LAZAREFF and LE BALLEUR method is a coupling viscous/inviscid method in which the outer flow interacts with a boundary layer on a wing. An analysis of the body influence on the inviscid flow around the wing is presented in section 4 by comparing results obtained using the multidomain method on the wing-fuselage configuration and on simplified configurations such as the wing mounted on an infinite cylinder and the exposed wing. In section 5, viscous effects are estimated on the wing alone using the coupling method ; the influence of the boundary layer on the outer flow is estimated from viscous and inviscid calculations, and typical boundary layer results are presented. Both viscous and body effects are discussed in transonic flow with some subsonic results also presented to show how these effects depend on the nature of the flow. A few additional remarks are made in section 6 about more empirical ways to explain remaining discrepancies between predicted and experimental results.

2 - TEST CASE : CONFIGURATION, EXPERIMENTAL SET-UP AND DATA -

Geometrical characteristics of the wing-body configuration.

The wing-body configuration used in this study is the DFLVR-F4 model [12]. It consists of a transonic wing of advanced technology mounted on an AIRBUS A310 fuselage. As shown in fig. 1, the F4 wing is of high aspect ratio (Λ = 9.5) with a crank at the trailing edge (0.4 b/2) ; the leading-edge sweep is 27.1° and the taper ratio 0.3. The basic airfoil [13] is supercritical with high rear loading The thickness to chord ratio varies from 0.15 at the root to 0.12 at the crank and remains constant up to the tip. The twist from the root to the tip is 5°. The wing is mounted in a low position with a dihedral of 4.8°.

Experimental set-up and techniques.

The experimental data used in this paper are from the S2MA transonic pressurized wind tunnel of the ONERA test center in Modane-Avrieux. The test section, 1.77 m high by 1.75 m wide, has perforated top and bottom walls with a 6 % maximum porosity, and solid side walls. Under these test conditions, wall interference corrections of the Mach number and angle of attack are very small.

The complete model (scale 1/30) was mounted on a Z-sting by means of a six component balance. 252 pressure taps were distributed into 7 spanwise sections on the right wing (η = 0.185, 0.238, 0.331, 0.409, 0.512, 0.636, 0.844) ; the instrumentation of the fuselage consists of 44 pressure taps in the symmetry plane. Dye injectors were implanted within the left wing. In order to ensure a shock wave turbulent boundary layer interaction at the test Reynolds number ($Re_{\bar{c}} = 3.10^6$ based on the reference aerodynamic chord $\bar{c}$ = 0.1412m), transition was tripped on the upper side (x/c = 0.05 / 0.15 / 0.05 resp. at the wing root, in the middle part, and at the tip), and on the lower side (x/c = 0.25 over the whole span) by a carborundum strip ; it was checked by means of an acenaphthene sublimation technique. Moreover, oil and dye visualizations were carried out and allowed to observe the boundary layer behaviour through the wall streamlines.

Test cases.

Two cases were selected for the calculation - experiment comparisons presented in this paper. The test parameters are :

M = 0.75 α = 0.10 $Re_{\bar{c}} = 3.10^6$
M = 0.60 α = 0.66 $Re_{\bar{c}} = 3.10^6$

The measured total lift coefficient is 0.50 in both cases. Fig. 2 shows the experimental pressure field in the transonic case. On the lower surface the strong aft loading with a maximum pressure located very close to the trailing edge must be noticed. The resulting large pressure difference between the two sides near the trailing edge is likely to be responsible for the limited separation appearing in the crank region on the upper side, which can be observed through the oil visualization (fig.3). The experimental pressure field in the subsonic case is shown in fig. 4. It should be noted that the adverse pressure gradient behind the suction peak developing very close to the leading edge led to a transition located upstream of the strip.

3 - COMPUTATIONAL METHODS -

Two ONERA computational methods were used in this study, both based on the same FPE solver. The inviscid flow field about the wing-body configuration can be calculated by a subdomain method, while the analysis of viscous effects on the wing alone is allowed by a coupling viscous / inviscid code.

3.1 - Basic FPE solver -

Governing equation

In a coordinate system (x,y,z) the full potential equation in nonconservative form can be expressed :

$$\mathcal{L}\,\Phi = 0$$

where $\mathcal{L}\Phi$ is given by :

$$\mathcal{L}\Phi = (a^2 - u^2)\,\Phi_{xx} + (a^2 - v^2)\,\Phi_{yy} + (a^2 - w^2)\,\Phi_{zz} - 2\,u.v\,\Phi_{xy} - 2\,u.w\,\Phi_{xz} - 2\,v.w\,\Phi_{yz}$$

and :

$$a^2 = \frac{1}{M_\infty^2} + \frac{\gamma - 1}{2}\,(1 - q^2)$$

where :

- Φ , is the velocity potential
- q , is the velocity vector of components (u,v,w) = grad Φ
- a , is the local sound speed
- M_∞ , is the freestream Mach number and
- γ , is the ratio of specific heats.

All of the variables are non-dimensionalized either by the modulus of the freestream velocity (U_∞) or by the half-span.

After some algebraic manipulation, this equation, in arbitrary curvilinear coordinate system is written :

$$\mathcal{L}\Phi = A\Phi_{\xi\xi} + B\Phi_{\eta\eta} + C\Phi_{\zeta\zeta} + D\Phi_{\xi\eta} + E\Phi_{\xi\zeta} + F\Phi_{\eta\zeta} + G = 0$$

where the curvilinear coordinates (ξ, η, ζ), a priori arbitrary, are those of the calculation space with a uniform rectangular grid, and where the coefficients A,B,C,D,E,F and G depend on the components of the velocity and of the metric, i.e.on the transformation derivatives from the calculation space (ξ, η, ζ) to the physical space (x,y,z).

Numerical algorithm

The numerical algorithm uses a finite-difference formulation developed by CHATTOT [2]. The second derivatives of the potential are approximated by central differences when the local flow is subsonic. When the flow is locally supersonic rotated differencing is ensured by a proper combination of central and upwind differences.

The resulting equations are solved by a column overrelaxation algorithm which can be written in the condensed form :

$$N(\omega)\,(\Phi^{m+1} - \Phi^m) = \omega\, L\Phi^m$$

where :

- Φ^{m+1}, is the vector of $\Phi^{m+1}_{i,j,k}$ values at the nodes at iteration m
- $L\Phi^m$, is the residue
- L , is a discretized form of $\mathcal{L}$
- ω , is the relaxation factor, with a value between 1 and 2 at a subsonic point and less than or equal to 1 at a supersonic point
- $N(\omega)$, is the iteration operator depending on all the values of ω (and of course the values of Φ^m).

3.2 - Subdomain method for inviscid wing-fuselage calculations -

Subdomain decomposition technique

The basic idea underlying this method [14,15,16] is to construct grid systems which are fitted for each component of the configuration. In this approach, the computational domain is divided into several overlapping subdomains, which are defined according to the different components of the configuration. Figure 5 shows a sketch of the decomposition of the flow field into two overlapping subdomains, a fuselage subdomain S_f and a wing subdomain S_W. The overlapping region is limited by two plane surfaces R_W and R_f which belong to the boundaries of the wing subdomain and of the fuselage subdomain respectively.

In each subdomain surface-fitted grids are generated separately with the minor restriction that R_W and R_f are mesh surfaces for both subdomains but with different distributions of mesh points for each subdomain.

The full potential equation is solved in non conservative form by the above mentioned SLOR algorithm, which is implemented independently in each subdomain.

In the present method using the Schwarz's alternating algorithm [17] the solution process is performed in cycles : it starts by calculating a solution for the flow field in wing subdomain. After a number of SLOR iterations, the distribution of velocity potential on R_f boundary is used as Dirichlet condition for calculation in the fuselage subdomain. Calculation of a solution in the fuselage subdomain is then started and a number of SLOR iterations are performed. This distribution of the velocity potential is used as a Dirichlet condition for the wing subdomain. This constitutes one cyle and the whole process is then repeated. Convergence is achieved when the error norm is below some given tolerance.

Grid generation

Grid generation for the two subdomains is based on two completely separate coordinate transformations. Second order accurate finite differences are used to evaluate the partial derivatives of the metrics so that the solution procedure is disconnected from the grid generation step.

Wing subdomain grid

Grid generation in wing subdomain is based on the so-called parabolic transformation which gives a two-dimensional grid of "C" type. The three-dimensional mesh is constructed by the usual way of stacking the two dimensional grids generated around selected spanwise sections of the wing.

Fuselage subdomain grid

In the present calculations, the fuselage is extended to infinity in the upstream and downstream directions by two circular cylinders which can be chosen with a small radius.

A grid of "H" type is constructed in each cross-section (constant-x plane) by a sequence of transformations which take into account the change in

the geometric shapes. Several cases are shown on fig. (6,a,b,c), corresponding to different sections of the F4 configuration :

- a cylindrical section (circular or non circular) with a cut or a sheet (fig. 6a),
- a section containing the fuselage and the leading edge of the wing, with a cut (fig. 6b),
- a section with a portion of the wing reaching the lateral boundary R_F (fig. 6c).

In each cross section, the grid is constructed with an upper and lower part and a connection is made in order to achieve the continuity of the mesh.

Figure 7 is a partial perspective view of the mesh system around the F4-AIRBUS wing/fuselage configuration. The figure shows the meshes on the wing, fuselage and wake, a part of the parabolic grid in a constant-y plane in the wing subdomain and the mesh in the plane of symmetry of the fuselage subdomain.

3.3 - Inviscid/boundary layer coupling method for viscous calculations -

Prediction of aircraft performances, particularly with advanced wings in transonic flow requires three-dimensional methods allowing more or less thoroughly for viscous effects ; works of FIRMIN [18], STREETT [19], WIGTON and YOSHIHARA [20], LAZAREFF and LE BALLEUR [21,22], ARTHUR [23] in this field must be mentioned.

The current approach used at ONERA was developed by LAZAREFF and LE BALLEUR [22]. It consists of coupling the above mentioned basic inviscid solver of the full potential equation with an integral method for three-dimensional laminar/turbulent boundary layers. At the moment this method is restricted to wing alone configurations. The inviscid mesh is fairly similar to that used in the wing subdomain of the above mentioned multidomain method. Modelling of viscous effects is restricted to the wing. In the present state of development of the method, viscous effects in the wake (displacement and curvature) are not allowed for. It is based on the defect formulation and the wall transpiration velocity concept. Outer velocities, necessary as input data to the boundary layer calculation, are provided by the potential calculation. Through the continuity equation, the boundary layer calculation yields the wall transpiration field, which is used as a boundary condition in the potential calculation. Fig. 8 shows an example of wall transpiration velocities on both upper and lower surfaces in the supercritical case investigated in this paper. The procedure is iterative, wall transpiration velocities being underrelaxed to ensure convergence of the coupling. The integral boundary layer method used at the present time is an extension of the approach of AUPOIX which is based on the COUSTEIX method [24]. Initial conditions for the boundary layer calculation are those of an infinite yawed cylinder (laminar case) ; flat plate approximations (laminar or turbulent) can also be used. Transition may be either enforced or calculated. In the latter case, it is determined after the Granville (longitudinal instability), Beasley (transverse instability) and Russell (transition at a separation bubble) criteria. In calculations presented in this paper, transition was enforced at the experimental transition location.

At transition only the momentum thickness is continuous. Although this method is restricted to attached flows, a numerical procedure (extrapolation of the wall transpiration velocities and smoothing in the extrapolated zones) prevents breakdown of the calculation when local separation occurs (as may happen during the first coupling iterations near the trailing edge).

4 - BODY EFFECTS ANALYSIS -

Processed configurations

The fuselage effect can be broken down into two parts : one part due to its shape in the intersection region, that of a cylinder on which the wing is mounted in low position ; the other, connected with the front and rear part, a finite body effect. To estimate each of these effects separately, one should compare the wing alone with the wing mounted on an infinite cylinder, and the latter with the wing-finite body configuration. For this purpose, three geometrical datasets were processed, each one yielding a different accuracy in the modelling of the actual configuration.

Fig.7 shows particular surfaces of grids modelling the wing mounted on the actual body. For the sake of clarity, coarse grids are shown in this figure. Actually, there are 170 x 20 x 30 nodes in the wing subdomain and 71 x 20 x 38 in the fuselage subdomain (in figure 7 respectively 44 x 20 x 10 and 35 x 20 x 38). The grid generation technique used in the body subdomain does not allow a strict closing of the forebody. However finite body effect can be modelled with some accuracy by using very small minimal values of the forebody radius.

The wing mounted in the same low position on an infinite cylinder was also processed. The grids used were similar around the middle part of the configuration which was unchanged. However, it should be noted that, as in most existing potential methods, the location of the wake must be that of a particular grid surface. When processing a non-symmetrical configuration, this constraint generally causes a deflection of the wake, which can clearly be seen in fig. 7. The authors are not convinced that this location is of no consequence as regards the computed solution. In this particular case, the infinite cylinder results in a smoother deflection than the finite body.

The multidomain program was also used as monodomain for calculating the wing alone, the boundary condition in the root plane being a symmetry condition. The grid was the same as the one used in the wing subdomain of the previous multidomain calculations (a deflection of the wake like that of the finite body case was artificially enforced). However, in the former cases, the inner part of the wing was lying in the body subdomain (cf. section 2) mapped by an "H" grid, while in the wing alone case, a single "C" grid is used, resulting in finer mesh spacing in the vicinity of the leading edge. These differences should be kept in mind when comparing results.

Results

Fig. 9 displays a system of calculated isomach lines on the upper side of the complete configuration in

the transonic case (M = 0,75 ; α = 0.1°). On the body, where the flow remains mostly subcritical, one may notice the expansion on the forebody extremity and the wing-induced acceleration in the middle part, starting from the wing root and lessening towards the symmetry plane. On the wing, a supersonic to supersonic shock wave grows stronger towards the tip, while a rear shock (supersonic to subsonic) degenerates into a weaker compression. The continuity is satisfactory across the overlapping region which is represented by the white strips in the picture. Pressure distributions in several wing sections are presented in fig. 10 for both finite and infinite body cases so as to illustrate the finite body effect. On the wing, it may be described as a general acceleration of the flow. In the very first sections by the root that do not exhibit any definite shock wave, suction levels are raised from the peak back to the trailing-edge ($\eta_{root} < \eta < 0.3$). The double shock structure in the following inner sections ($0.3 < \eta < 0.5$) is affected by the finite body : the weak supersonic to supersonic shock shifts backwards and the following expansion and rear supersonic to subsonic shock are reinforced. On the outer wing ($\eta > 0.5$), the unique strong shock shifts backwards : the finite body effect thus spreads over the full span. This effect is weaker on the lower side : pressures decrease near the root, more noticeably in the expansion region, but the effect rapidly fades away towards the outer wing. Fig. 11 is an illustration of the whole body effect : it compares pressure distributions from the actual configuration and wing alone calculations. The comparison is roughly similar to the former one, particularly with respect to the shock position. This result indicates that an infinite body modelling is not decidedly more accurate than a wing alone approximation of the actual configuration ; in the present case the forebody effect is dominant. However, the cylinder effect shown in figure 12 is not negligible in inner sections. Near the root, pressures significantly increase on both upper and lower side in the first 70 % of the chord when the wing is mounted on a cylinder ; in the rear part a slight lessening of the lower side pressure may be noticed while the upper surface pressure remains unchanged. Superposition of this effect with that of the finite body results in the actual body effect shown in fig.11. It may be noted that near the root, the overall effect is weaker than eitherof its components because they somewhat oppose one another, particularly in the first two thirds of the chord. The overall effect can be roughly described as a drop in pressure in the trailing edge area. No conclusions can be drawn from the suction peak being more acute in the wing alone case because this obviously is a consequence of above mentioned local differences in mesh density around the leading edge.

Since the main phenomenon due to the body presence in this transonic case seems to be an alteration of the shock pattern, an essentially subsonic case without any shock wave has also been investigated. The actual configuration and the exposed wing have been calculated at a Mach number of 0.60 and an angle of attack of 0.66°. Pressure distributions are compared in fig.13. On the lower side, the body effect is the same as in the transonic case (because the flow remained subcritical there). In inner sections on the upper side, pressures are lessened in the rear part of the wing by the fuselage effect ; in middle sections, they are uniformly diminished from the suction peak back to the trailing edge ; further toward the outer wing the effect fades away.

Up to this point of the study, experimental results were left aside because they did not allow an estimation of the body effect. But if calculated results on the actual configuration (wing + finite body) are compared to experiment at the same angle of attack, they show very poor agreement. Fig.14 presents pressure distributions on the wing, and fig.15, on top and bottom of the fuselage. In inner wing sections, the predicted forward shock is smeared while the rear shock is too strong when compared with experiment. In outer sections, the predicted shock lies downstream of the experimental one. The rear loading is overestimated and so are pressure levels on the lower side of the outer wing. Most of these discrepancies are typical of intense viscous effects, which are neglected by the calculation. The inviscid approach thus seems to fail to predict an accurate solution, whether or not the body is correctly modelled. Thus the viscous transonic investigation of the flow presented in section 5 is called for.

5 - VISCOUS EFFECTS ESTIMATION -

Viscous calculations of the wing alone configuration were carried out using the LAZAREFF and LE BALLEUR method . Without going into the details of the procedure, it may be noted that a sequence of two grids is used to accelerate convergence of the calculation. The coarser one is chosen fine enough to yield an inviscid predictor with a sufficient circulation level. Coupling is then carried out in the final 172 x 29 x 30 mesh. One coupling cycle consists of one three-dimensional boundary layer calculation followed by 50 iterations of the inviscid method. A relaxation factor of ω = 0.4 for the transpiration velocities ensures fast convergence of the coupling.

The first result concerns the transonic case at a Mach number of M = 0.75 and an angle of attack of α = 0.1° ; the Reynolds number based on the aerodynamic chord is 3.10^6. Transition is enforced on both sides at the location of the experimental transition strip (cf § 2). The comparison between experimental and theoretical pressure fields in fig.16 shows that taking viscosity on the wing into account significantly improves prediction. On the upper side the viscous calculation yields a shock location nearer to the experimental position ; particularly it should be observed that viscosity reduces velocity levels downstream from the shock and suppresses the flow expansion predicted in this area by the inviscid calculation. On the lower side viscous effects appreciably reduce the aft loading and slightly accelerate the flow on the whole surface. Yet experimental pressure levels over the lower side could not be accurately predicted even if this acceleration were combined with that caused by the body (cf. §4). Moreover, the comparison between theoretical and experimental results shows considerable discrepancies concerning the trailing edge pressure levels, since the calculation yields pressures that are too high. Possible causes of these poor correlations will be investigated in section 6. Fig.17 shows the spanwise lift variation, $\Delta C_\ell / C_\ell = (C_\ell - C_{\ell\,wa,inviscid}) / C_{\ell\,wa,inviscid}$ due to the viscous effects on the one hand and the fuse-

lage on the other hand, as compared with the lift variation corresponding to a perfect prediction of the experimental results ; the remaining curve in the graph (aeroelastic deformation) will be discussed in section 6. This comparison shows that the lift reduction due to viscous effects is at least four times stronger than the rise due to the fuselage, and substantially improves the prediction. However the remaining lift discrepancies between theory and experiment are still great and may be partly related to the poor lower side pressure prediction.

Calculated values of the shape parameter H_i, streamwise momentum thickness θ_{11}, limiting wall streamline angle β , allow an estimation of the strength of viscous effects and the eventual imminence of separation. On the upper side of the wing compression through the shock wave remains moderate and does not perturb the boundary layer development very much : due to the shock Hi reaches a maximum value of 1.62 on the outer wing (fig.18a). On the other hand the boundary layer undergoes a pronounced thickening near the trailing edge (fig.18b), where Hi reaches values of over 2.2. Angle β increases very steeply in the last 20 % of the chord (fig.18c). The increase in calculated viscous effects is thus very steep at the upper side trailing edge. On the lower surface, the airfoil rear camber has an obvious influence on the boundary layer behaviour. The boundary layer causes a decambering of the profile which leads to a loss of lift. Moreover the maximum relative momentum thickness is 35 % greater at the wing tip than at the root (fig.19b) ; the shape parameter Hi and angle β reach maximum values of resp. 1.81 (fig.19a) and 36° (fig.19c) at the tip. In fig.20, calculated values of the angle $(\alpha_e+\beta)$ between the wall streamlines and the upstream flow direction are plotted against experimental values. The latter were provided by oil visualizations. It may be observed that the calculation yields a qualitatively correct reproduction of the streamlines deviation in the aft highly loaded area, chordwise as well as spanwise. In particular the steep spanwise increase of $(\alpha_e+\beta)$ outwards from the crank (η=0.4) is correctly predicted.

The second result concerns a subsonic case, at a Mach number M = 0.60 and an angle of attack α = 0.66 The Reynolds number is 3.10^6. On the lower side transition is enforced at x/c = 0.15 over the whole span, as in the experiment. On the upper side, transition is enforced at the separation bubble behind the suction peak. A comparison between calculated and experimental pressure fields is shown in fig.21. On the upper side velocities are lessened over the whole surface when viscosity is accounted for, which means improvement of the theory-experiment agreement.

As in the transonic case, viscous effects calculated on the lower side are mainly perceptible in the aft loading region and they not entirely make up for the discrepancy between theory and experiment as regards the spanwise lift distribution (fig.22). It is worth noting that the loss of lift due to viscous effects is greater in a transonic flow than in a subsonic flow (fig.23). The additional loss may be ascribed to the shift in shock position due to viscous effects.

While no apparent improvement of the agreement between experimental and theoretical results could be obtained by taking fuselage effects into account (cf. §4) under the inviscid hypothesis, an essential improvement results from allowing for viscous effects, which are, in this case, much stronger than body effects in terms of lift. Moreover, among the remaining discrepancies, the still unaccurate trailing edge pressure prediction would probably be improved by a more complete viscous approach including viscous modelling of the wake. The discrepancies in the pressure fields on the lower side of the wing will be discussed in section 6. It should also be noted that the viscous "wing alone" modelling used in this section did not include wing junction effects as regards the boundary layer.

6 - ADDITIONAL REMARKS ABOUT EXPERIMENT - THEORY CORRELATION -

Aeroelastic deformation

Successes and failures of potential flow codes in transonic wing design have been thoroughly discussed by HICKS [10]. Together with inviscid and wing alone approximations, this author has mentioned aeroelastic deformation among factors likely to cause poor experiment - theory correlation, particularly for high aspect ratio wings. Calculations presented in sections 4 and 5 were carried out using the theoretical wing geometry ie assuming that there was no deformation. However, a corrected twist distribution was calculated by NLR to account for the deformation of the model in the wind tunnel at a Mach number of 0.75 and a total lift coefficient of 0.50. A maximum twist correction of - 0.4° at the wing tip was estimated. The effect of this deformation on the calculated flow has been evaluated by inviscid wing alone calculations on both theoretical and corrected wings. Results are presented in fig.17, in terms of spanwise lift variation. In this particular case the calculated effect is not strong enough to basically modify the previously mentioned experiment - theory discrepancies. In particular, lower side pressure levels were not significantly altered by the geometrical correction.

Trailing edge treatment

Experimental observations have shown that the wing trailing edge is affected by a slight separation (cf §2). The large pressure difference between the upper and lower surface close to the trailing edge (due to the rear loading maximum pressure being located very close to the trailing edge) is likely to induce this separation by forcing the flow to go around the trailing edge, as was shown by Körner and Redeker [25] ; DFVLR have thus modified the basic airfoil of the F4 wing so as to shift the maximum pressure away from the trailing edge (from x/c =.95 to x/c =.85) ; drag and dragrise performances were noticeably improved [25], thus showing that the shape of the rear loading has a noticeable influence on the aerodynamic behaviour of the airfoil.

On account of these observations, two limitations of the computational methods used in this study may be underlined. In the first place, the coupling method is restricted to essentially attached flows. However as the local separation at the trailing edge is unrelated to the upper surface boundary layer evolution, the approach is probably still valid with respect to this point. Secondly, the wake position cannot be calculated : it is enforced beforehand. Calculations presented in sections 4 and 5 were carried out with a wake leaving the trailing edge with a bisector orientation ; although this is a rather usual way, it should be noted that some

authors choose a lower surface orientation when a shock wave develops on the upper surface [26,27]. In a coupling method including viscous wake modelling the wake position should be part of the calculated solution [28]. Such a three-dimensional method being unavailable for the present study, an empirical hypothesis has been attempted. The large pressure difference near the trailing edge connected with the flow going around the trailing edge probably causes a deflection of the wake from the bisector orientation. In the absence of any certain knowledge of the wake orientation, either theoretical or experimental, the condition chosen was that of equal pressures on both sides of the trailing edge at the last grid points on the wing. This equality condition is consistent with the observed tendency for the flow to go around the trailing edge. The wake orientation was calculated iteratively so that this condition would be fulfilled. Results shown in fig.24 and 25 were obtained by a viscous calculation of the theoretical geometry (without aeroelastic correction) with the modified wake position; calculated values of the deviation between the wake and the trailing edge bisector were from 4° to 8°. They show consistent improvement of the prediction of lower surface pressure levels and lift distribution when compared to the viscous results with a bisector wake. These results, although they are based on a particular and debatable hypothesis indicate that a potential solution may highly depend on the trailing edge treatment as regards the wake orientation. Since this treatment is simplified in most existing methods either inviscid or coupled without complete wake modelling, it may be a source of uncertainties.

7 - CONCLUSION -

Inviscid fuselage influence and viscous effects on the wing of the DFVLR-F4 typical advanced transport aircraft configuration in transonic flow were separately estimated using two computational methods based on the potential equation, and able to model these effects.

Body effects were found to be moderate and essentially due to the forebody ; they mainly consist of a shift in the shock position on the upper surface.

Very significant viscous effects were calculated thus allowing a considerable improvement of the prediction.

The agreement between experimental and theoretical results was further improved by attempts to allow for particular physical phenomena such as aeroelastic deformation and more realistic wake position.

These results indicate that transonic flow prediction about wing-body configurations neglecting body modelling and viscous effects can be substantially improved by more accurate theoretical treatment. A sound theoretical approach should include proper modelling of the geometrical features and make a thorough allowance for viscous effects (strong coupling). In particular a viscous wake model would be necessary to determine the viscous effects of the wake (displacement and curvature) and its position which was shown to influence the solution.

REFERENCES

[1] JAMESON,A.
"Iterative solution of transonic flows over airfoils and wings, Including Flows at Mach 1"

Comm. on Pure and Applied Math.,Vol.27, 1974, pp. 283-309.

[2] CHATTOT J.J., COULOMBEIX C. and DA SILVA TOME C.
"Calculs d'écoulements transsoniques autour d'ailes",
La Recherche Aérospatiale n°4,1978,pp.143-159
English Translation ESA-TT-561.

[3] CAUGHEY D.A. and JAMESON A.
"Numerical Calculation of Transonic Potential Flow About Wing-Body Combinations"
AIAA Journal, Vol.17,n°2, February 1979,pp. 175-181.

[4] BAKER T.J. and FORSEY C.R.
"A fast Algorithm For The Calculation Of Transonic Flow Over Wing/Body Combinations".
AIAA Fith Computational Fluid Dynamics Conference, Palo Alto, Ca., June 1981.

[5] THOMAS S.D. and HOLST T.L.
"Numerical Computation of Transonic Flow about Wing-Fuselage Configurations on a Vector Computer"
AIAA Paper 83-0499, 1983.

[6] BOPPE C.W. and STERN M.A.
"Simulated Transonic Flows for Aircraft with Nacelles, Pylons and Winglets"
AIAA Paper 80-130, 1980.

[7] WAGGONER E.G.
"Computational Analysis for an Advanced Transport Configuration with Engine Nacelles"
AIAA Paper 83-1851, 1983

[8] JAMESON A. and BAKER T.J.
"Solution of The Euler Equations For Complex Configurations"
AIAA Paper 83-1929, 1983.

[9] HOLST T.L., SLOOFF J.W., YOSHIHARA H., BALLHAUS W .F.,
"Applied Computational Transonic Aerodynamics"
AGARDograph n°266, 1982 .

[10] HICKS R.M.
"Transonic Wing Design Using Potential-Flow Codes. Successes and Failures"
SAE Paper n° 810565, 1981.

[11] SCHMITT V.
"Aerodynamique d'un ensemble voilure-fuselage du type avion de transport"
Colloque d'Aérodynamique Appliquée de l'AAAF, Poitiers, Novembre 1981.

[12] REDEKER G., MULLER R.
"Design and experimental verification of two supercritical Airfoils"
GARTEUR/DGLR Symp. "Transonic Configurations"
Bad Harzburg FRG,June 1978, DGLR n°78-075.

[13] REDEKER G., SCHMIDT N., MULLER R.
"Design and experimental verification of a transonic wing for a transport aircraft"
AGARD-CP-285, Paper n°13, 1980.

[14] LÊ T.H.
"Transonic Potential Flow Calculation About Complex Bodies by a Technique of Overlapping Subdomains"
8th Conf. Internationale sur les méthodes numériques en Dynamique des Fluides, Aix-la-Chapelle, Lecture Notes in Physics, Vol.170 (1982), pp.308-314.

[15] LÊ T.H.
"Calculs d'écoulements transsoniques autour d'une configuration Aile-Fuselage dans une Approche par Domaines"
La Recherche Aérospatiale, n°1983-3, 1983, pp. 175-186.

[16] LÊ T.H.
"A subdomain decomposition Technique as an Alternative for Transonic Potential Flow Calculations Around Wing-Fuselage Configurations"
5th GAMM Conference on Numerical Methods in Fluid Dynamics, Rome, october 1983.

[17] SCHWARZ H.A.
Gesammelte Mathematische Abhandlungen,Vol.2, pp. 133-134, Berlin, Springer 1890.

[18] FIRMIN M.C.P.
"Calculations of Transonic Flow over wing-body combinations with an allowance for viscous effects"
AGARD CP-291, paper n°8, 1981.

[19] STREET C.L.
"Viscous-inviscid interaction for transonic wing-body configurations including wake effects"
AIAA Paper 81-1266, 1981.

[20] WIGTON L.B. and YOSHIHARA H.
"Viscous inviscid interactions with a three-dimensional inverse boundary layer code"
2nd Symp. on Numerical and Physical Aspects of Aerodynamic Flows,California State University, Long Beach, USA,January 1983.

[21] LE BALLEUR J.C.
"Numerical Viscid-Inviscid Interaction in steady and Unsteady Flows".
2nd Symposium on Numercial and Physical Aspects of Aerodynamics Flows, Long Beach (Calif.) January 1983.

[22] LE BALLEUR J.C., LAZAREFF M.
"Computation of three-dimensional viscous flows on transonic wings via boundary layer inviscid flow interaction". La Recherche Aérospatiale, n°1983-3, 1983.

[23] ARTHUR M.T.
"A method for calculating subsonic and transonic flows over wings or wing-fuselage combinations with an allowance for viscous effects". AIAA Paper 84.0428, 1984.

[24] COUSTEIX J.
"Analyse théorique et Moyens de prévision de la couche limite tridimensionnelle". Note Technique ONERA n°157, 1974, english translation ESA.TT.238.

[25] KORNER H. and REDEKER G.
"Recent Airfoil Developments at DFVLR"
ICAS Paper 82.5.6.2., 1982.

[26] VAN DER VOOREN J., VAN DER KOLK J.TH. and SLOOFF J.W.
"A system for the numerical simulation of sub- and transonic viscous attached flows around Wing-Body Configurations". AIAA Paper 82.0935, 1982.

[27] MANGLER K.W. and SMITH J.H.B.
"Behaviour of the vortex sheet at the trailing edge of a lifting wing",
RAE TR 69049, 1969.

[28] LE BALLEUR J.C.
"Calcul par couplage fort des écoulements visqueux transsoniques incluant sillages et décollements. Profils d'ailes portants",
La Recherche Aérospatiale, N°3, 1981 pp.161-185

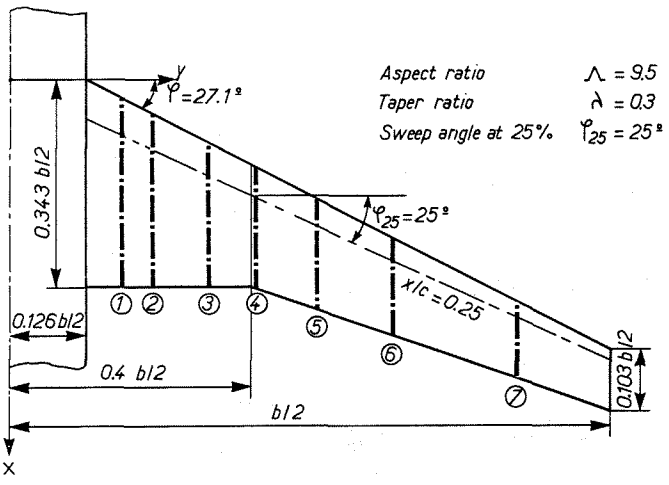

Fig. 1 - DFVLR-F4 wing planform

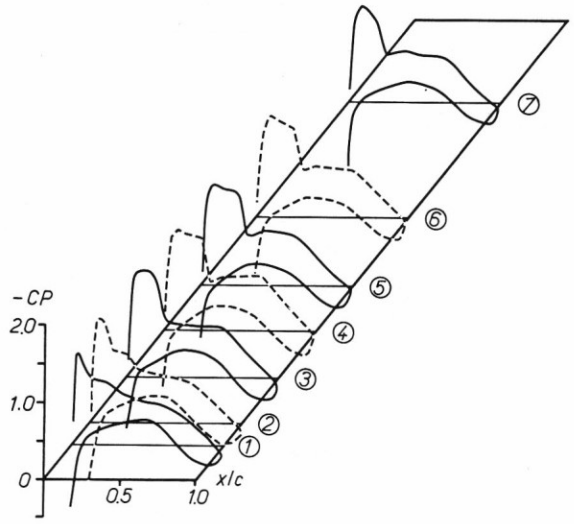

Fig. 2 - Experimental pressure distributions ($M = 0.75$; $C_L = 0.50$; $Re_{\bar{c}} = 3 \times 10^6$).

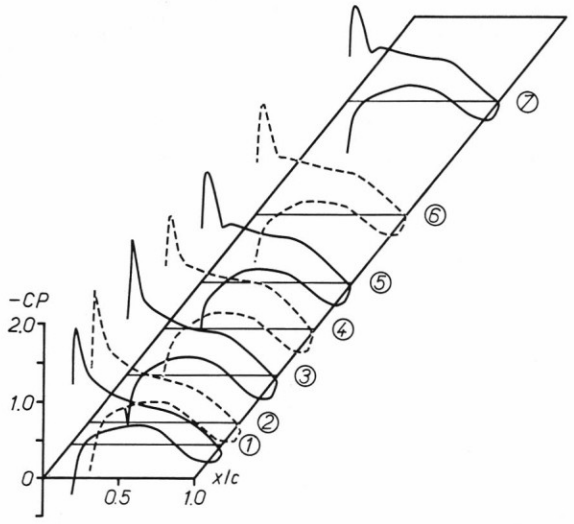

Fig. 4 - Experimental pressure distributions ($M = 0.60$; $C_L = 0.50$; $Re_{\bar{c}} = 3 \times 10^6$).

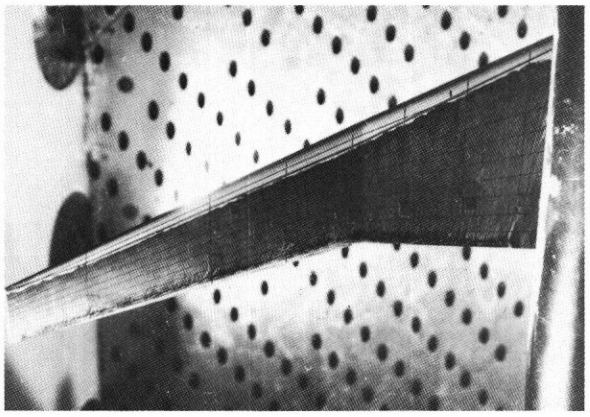

Upper side

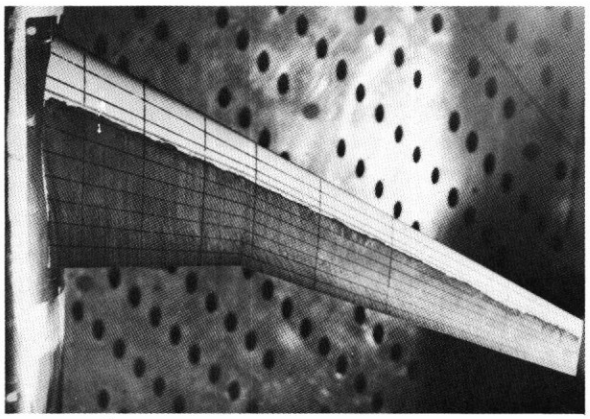

Lower side

Fig. 3 - Wall streamlines visualization ($M = 0.75$; $C_L = 0.50$; $Re_{\bar{c}} = 3 \times 10^6$).

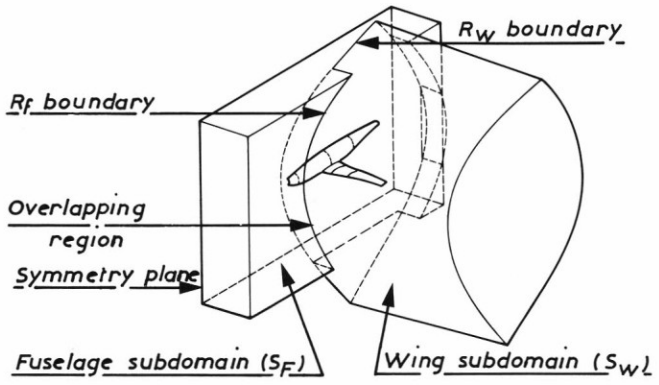

Fig. 5 - Sketch of the decomposition into wing and fuselage subdomains.

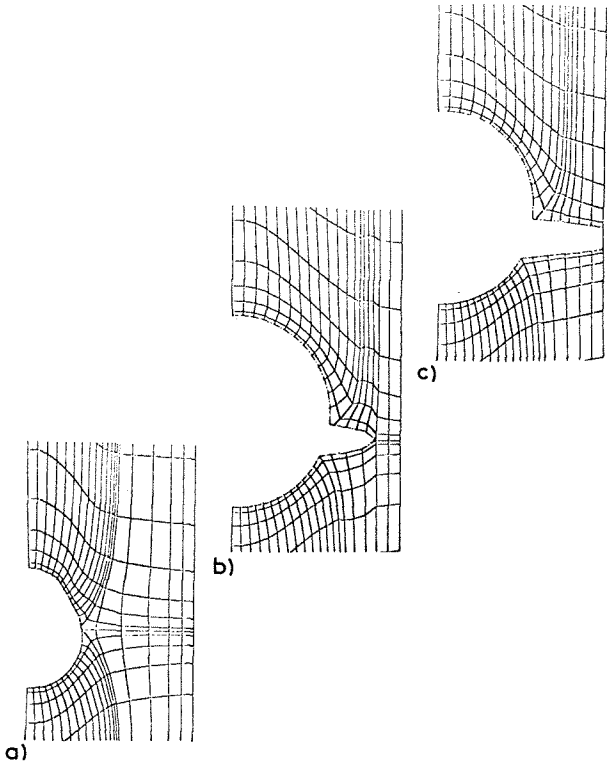

Fig. 6 - Fuselage subdomain grid system.

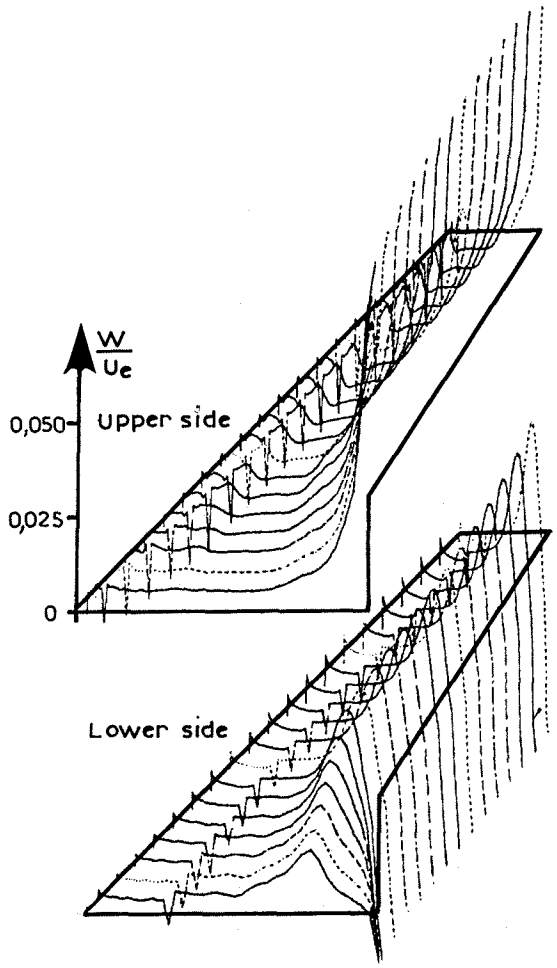

Fig. 8 - Wall transpiration velocity distributions ($M = 0.75$; $\alpha = 0.1^{\circ}$; $Re_{\overline{c}} = 3 \times 10^6$).

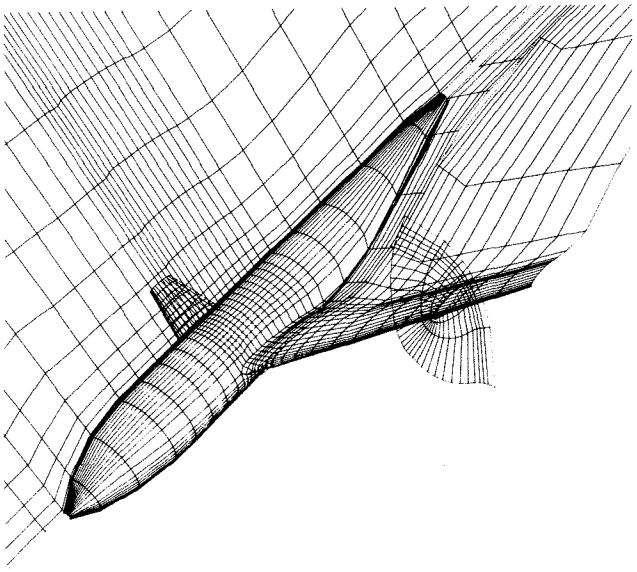

Fig. 7 - Perspective view of the wing-fuselage coarse mesh system.

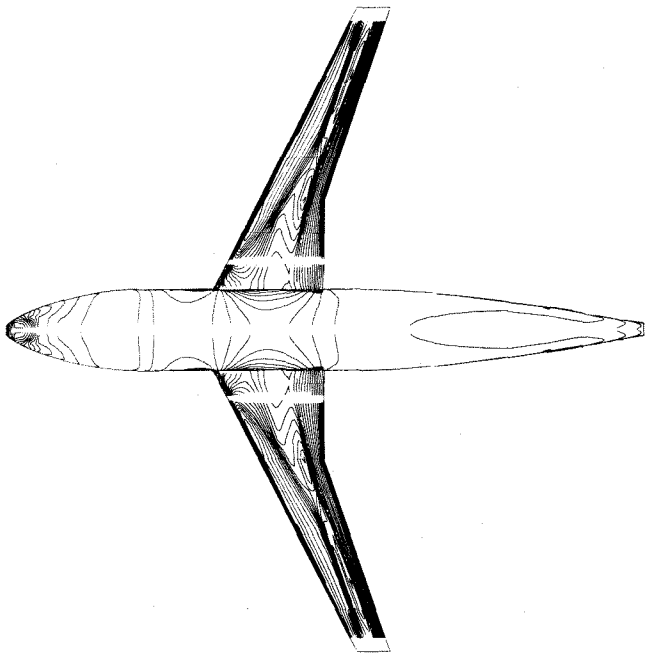

Fig. 9 - Calculated isomach lines on the upper surface of the wing-fuselage configuration. ($M = 0.75$; $\alpha = 0.1°$).

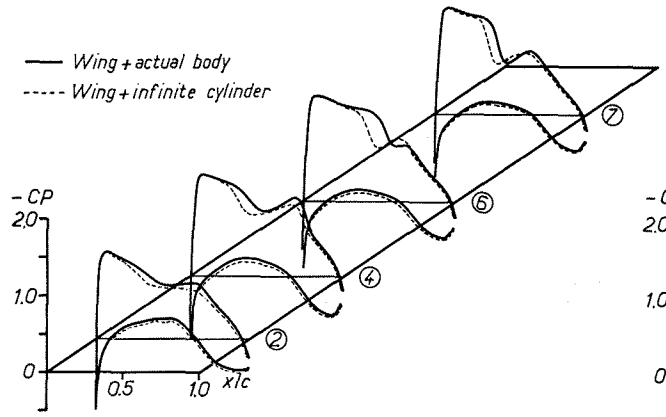

Fig.10 - Chordwise pressure distributions on the wing ; forebody effect. (M = 0.75 ; α = 0.1°).

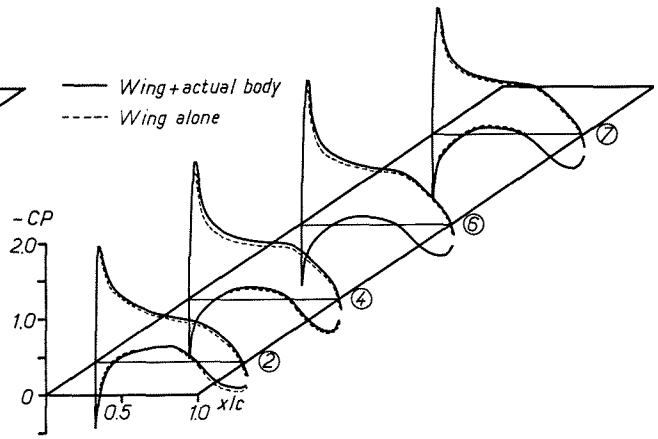

Fig.13 - Chordwise pressure distributions on the wing ; body effect. (M = 0.60 ; α = 0.66°).

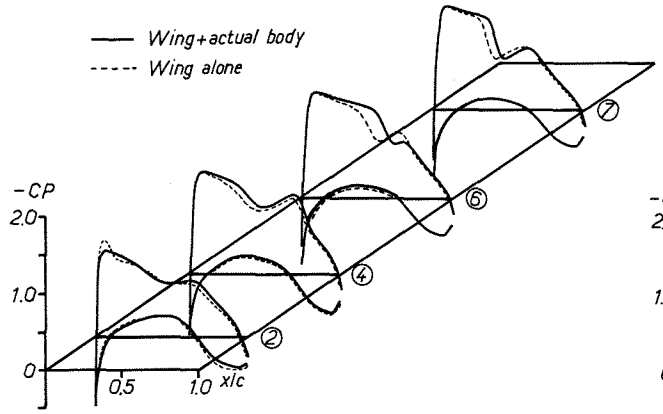

Fig.11 - Chordwise pressure distributions on the wing ; body effect. (M = 0.75 ; α = 0.1°).

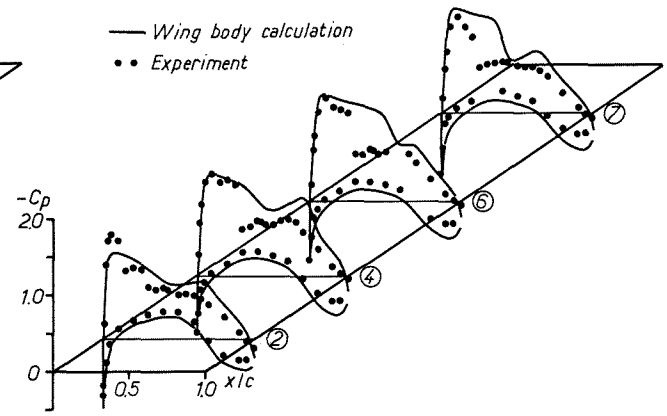

Fig.14 - Chordwise pressure distributions on the wing. (M = 0.75 ; α = 0.1°).

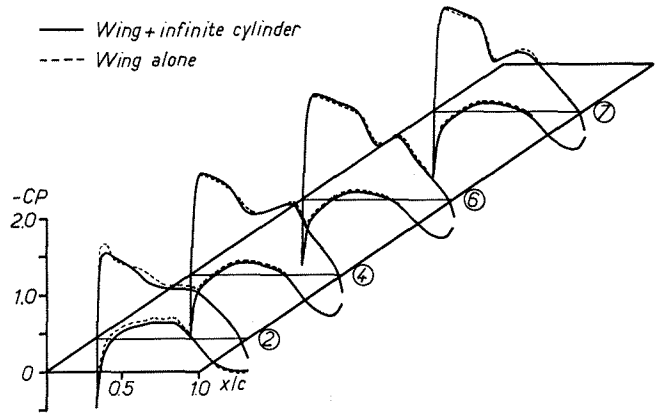

Fig.12 - Chordwise pressure distributions on the wing ; infinite body effect. (M = 0.75 ; α = 0.1°).

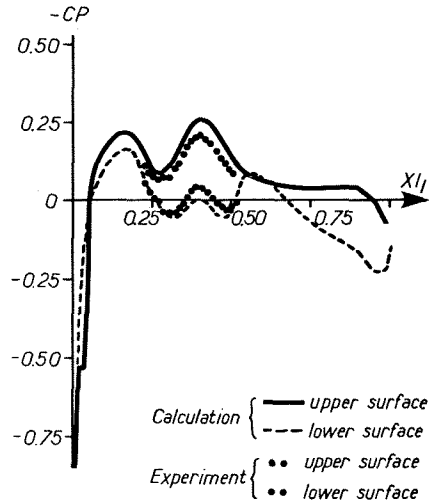

Fig.15 - Body pressure distributions in the symmetry plane. (M = 0.75 ; α = 0.1°).

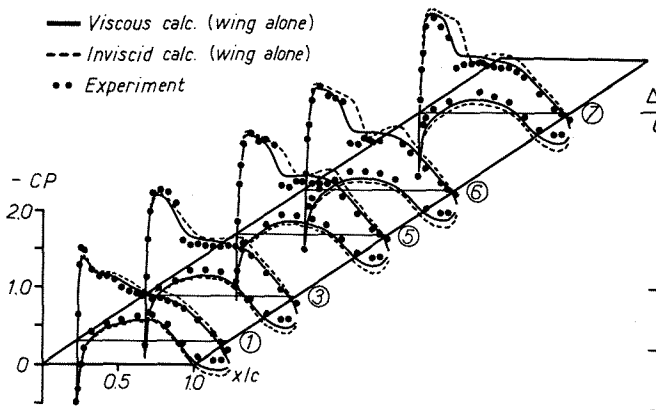

Fig.16 - Chordwise pressure distributions on the wing ;viscous effect.
(M = 0.75 ; α = 0.1° ; $Re_{\overline{c}}$ = 3 x 10^6).

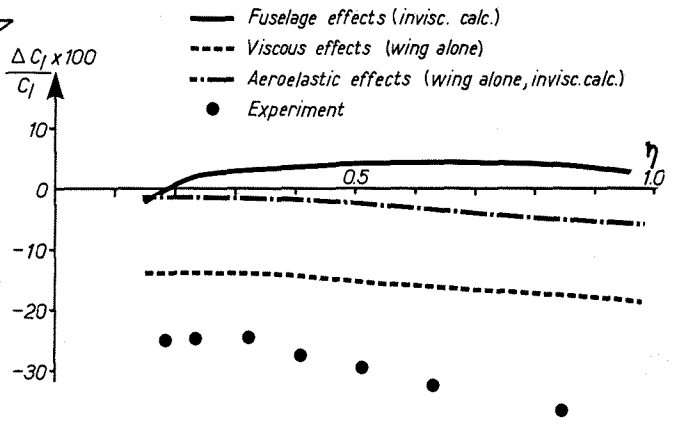

Fig.17 - Spanwise lift reduction parameter.
(M = 0.75 ; α = 0.1° ; $Re_{\overline{c}}$ = 3 x 10^6).

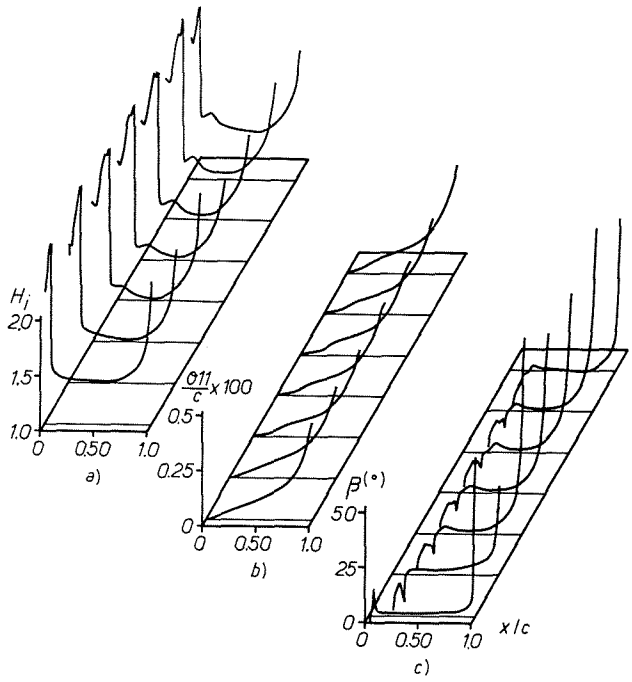

Fig.18 - Boundary layer characteristics on the upper surface.
(M = 0.75 ; α = 0.1° ; $Re_{\overline{c}}$ = 3 x 10^6).

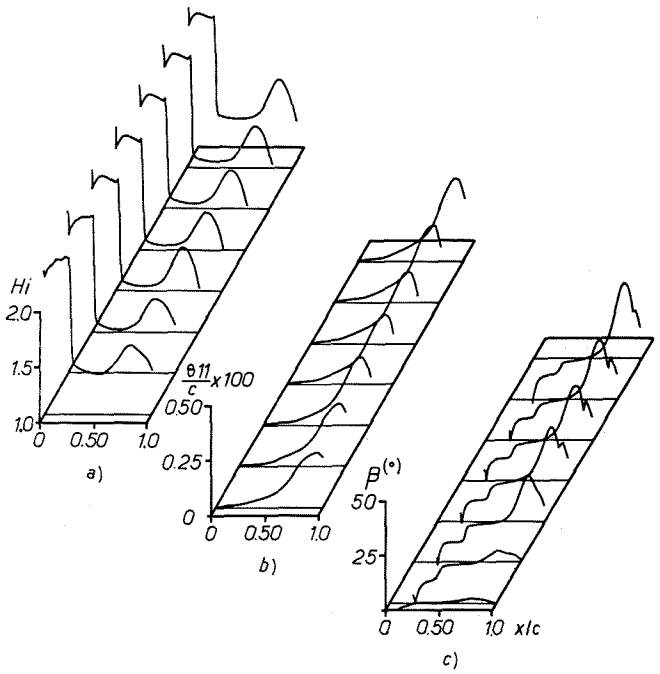

Fig.19 - Boundary layer characteristics on the lower surface.
(M = 0.75 ; α = 0.1° ; $Re_{\overline{c}}$ = 3 x 10^6).

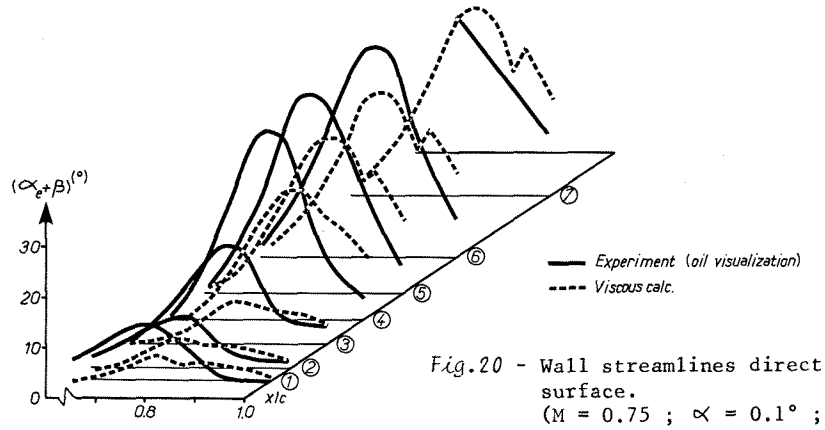

Fig.20 - Wall streamlines direction on the lower surface.
(M = 0.75 ; α = 0.1° ; $Re_{\overline{c}}$ = 3 x 10^6).

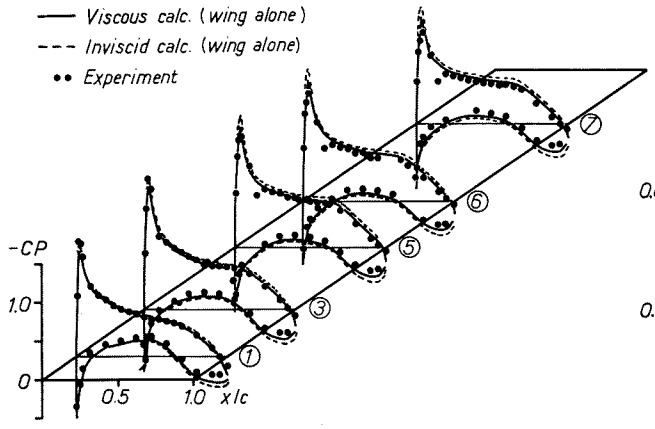

Fig.21 - Chordwise pressure distributions on the wing ; viscous effect.
(M = 0.60 ; α = 0.66° ; Re_c = 3 x 10^6).

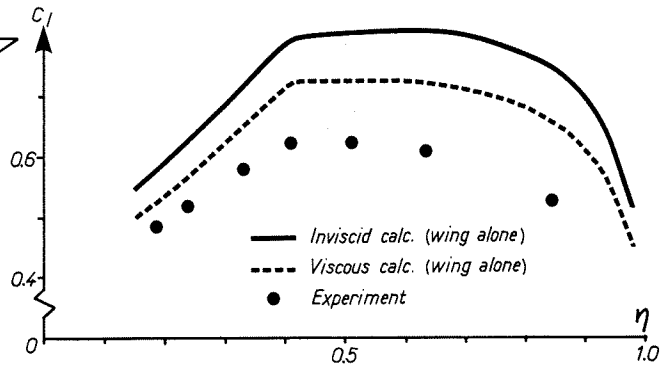

Fig.22 - Spanwise lift distribution, viscous effect.
(M = 0.60 ; α = 0.66° ; Re_c = 3 x 10^6).

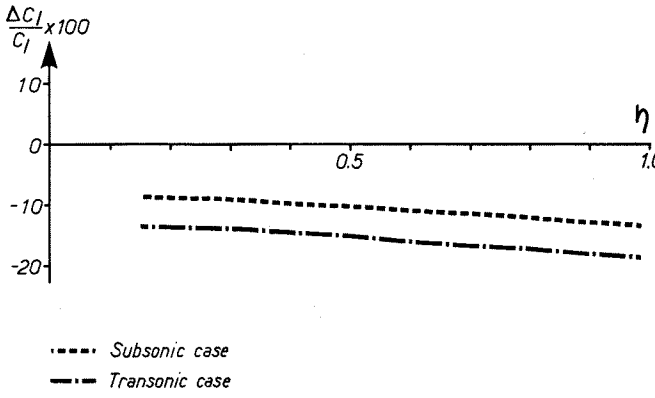

Fig.23 - Spanwise lift reduction parameter, computed viscous effect.

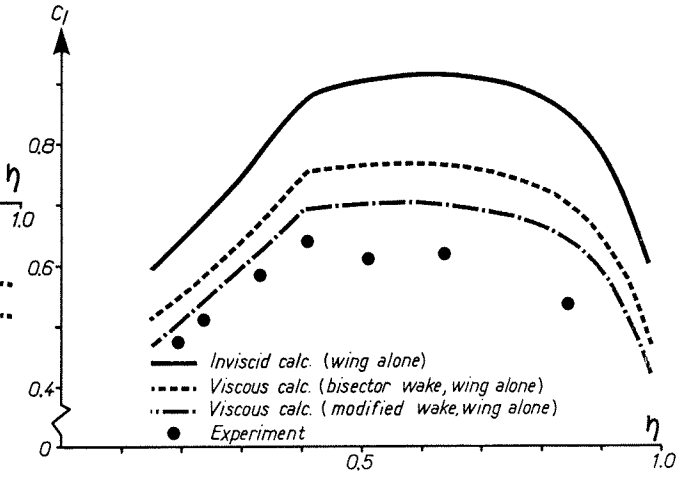

Fig.24 - Spanwise lift distribution.
(M = 0.75 ; α =0.10° ; Re_c 3 x 10^6).

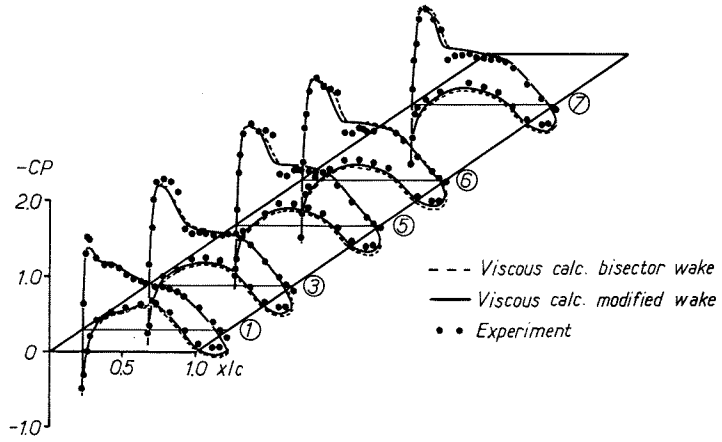

Fig.25 - Chordwise pressure distributions on the wing ; wake orientation effect.
(M = 0.75 ; α = 0.1° ; Re_c = 3 x 10^6).